

Cite this article as: Deng Chengjun, Lin Fukai, Yang Tianen, et al. Erosion-Corrosion of Ti(C, N)-Mo₂C-Ni Cermet and WC-Co Cemented Carbide in Alkaline Conditions[J]. Rare Metal Materials and Engineering, 2025, 54(04): 886-897. DOI: <https://doi.org/10.12442/j.issn.1002-185X.E20230048>.

ARTICLE

Erosion-Corrosion of Ti(C, N)-Mo₂C-Ni Cermet and WC-Co Cemented Carbide in Alkaline Conditions

Deng Chengjun^{1,2,3}, Lin Fukai³, Yang Tianen^{3,4}, Hong Huaping⁴, Liang Lei³, Peng Huabei³, Xiong Ji³

¹Chongqing Engineering Technology Research Center for Light Alloy and Processing, Chongqing Three Gorges University, Chongqing 404100, China; ²Chongqing Engineering Research Center for Advanced Intelligent Manufacturing Technology, Chongqing Three Gorges University, Chongqing 404100, China; ³College of Mechanical Engineering, Sichuan University, Chengdu 610065, China; ⁴Ningbo Sanhan Alloy Materials Co., Ltd, Ningbo 315311, China

Abstract: Ti(C, N)-Mo₂C-Ni cermet as alternative materials was explored for use in alkaline conditions, replacing the WC-Co cemented carbides, since Co is classified as a potentially carcinogenic substance and there is potential hazard of “hard metal disease” under the exposure to cobalt dust. The changes in microstructure, corrosion rate and volumetric loss rate of the two materials were compared under electrochemical corrosion and erosion-corrosion in alkaline environment. The results demonstrate that Ti(C, N)-Mo₂C-Ni cermet undergoes passivation when exposed to electrochemical corrosion of NaOH solution, resulting in a significant increase in oxygen content on the corroded surface. The corrosion rate of cermet is approximately one order of magnitude lower than that of the cemented carbide. Under the erosion-corrosion of an alkaline sand-water mixture, both the cermet and cemented carbide experience a gradual increase in volumetric loss rate with prolonging the erosion time. During erosion, the rim phase in cermet is fragile, so cracks easily penetrate it while the core phase remains intact. The medium-grained cemented carbide commonly demonstrates transgranular fracture mode, while in the fine-grained cemented carbide, cracks tend to propagate along phase boundaries. The erosive wear and damage caused by sand particles play a predominant role in the erosion-corrosion process of alkaline sand-water mixtures. This process represents an accelerated destructive phenomenon influenced and intensified by the combined effects of corrosion and erosion. It is confirmed that using cermet as an alternative anti-wear material to cemented carbides is feasible under alkaline conditions, and even better.

Key words: cermet; cemented carbide; erosion-corrosion; electrochemical corrosion; alkaline conditions

1 Introduction

Industrial wastewater treatment has gained increasing attention due to its association with environmental protection and resource recycling^[1]. Alkaline wastewater from chlor-alkali plants is a hazardous waste that poses challenges due to its strong corrosiveness. In the primary wastewater treatment, the anti-wear materials used in centrifuge spiral blade components play a crucial role. They are subjected to multiple forms of damage, including electrochemical corrosion due to different phases and composition, high-speed liquid flushing,

sand particle impact, and frictional wear in alkaline wastewater. These demanding conditions impose high performance requirements for anti-wear materials.

Ceramic materials possess excellent corrosion resistance and wear resistance. However, when subjected to high-speed impacts from sand particles in wastewater, ceramic materials tend to fracture and fail due to their inherent brittleness. To address this limitation, high-toughness metal was incorporated into ceramics to improve the toughness and resistance to fracture. Among ceramic-based composite materials, WC-Co cemented carbide, mainly used as cutting tool material^[2], is

Received date: April 13, 2024

Foundation item: Chongqing Light Alloy Materials and Processing Engineering Technology Research Center Open Fund Project (GCZX201903); Yunnan Province Major Science and Technology Special Project Plan (202302AA310038); Sichuan University-Suining Municipal-University Cooperation Project (2023CDSN-12)

Corresponding author: Yang Tianen, Ph. D., Associate Professor, College of Mechanical Engineering, Sichuan University, Chengdu 610065, P. R. China, E-mail: yangtze86@scu.edu.cn

Copyright © 2025, Northwest Institute for Nonferrous Metal Research. Published by Science Press. All rights reserved.

used as an anti-wear material for the components of centrifuge spiral blades. WC-Co cemented carbide possesses comprehensive mechanical properties such as high strength, high hardness, high fracture toughness, and wear resistance^[3-4]. Research has been carried out to improve the corrosion resistance of cemented carbides by introducing additives or modifying the composition of binders. Tang et al^[5] enhanced the anti-corrosion properties of WC-Co cemented carbides by incorporating aluminum (Al) based on calculated resulting phase and Pourbaix diagrams. In addition, they performed experiments in 3.5wt% NaCl electrolyte to verify the effectiveness of anti-corrosion properties. Results revealed that at Al content of 0.8wt%, the corrosion current density significantly decreased by two orders of magnitude. Moreover, the charge transfer resistance doubled, and the binder phase exhibited reduced damage, reflecting a notable improvement in corrosion resistance. Li et al^[6] introduced varying amounts of rhenium (Re) into WC-15Co cemented carbides and assessed the impact on anti-corrosion properties. The results revealed a non-linear relationship between Re content and corrosion resistance. Initially, as the Re amount increased, the anti-corrosion ability of the cemented carbides improved. However, beyond a certain point, it started to decline. Specifically, when the Re content reached 4.5wt% in HCl solution and 3.0wt% in NaOH solution, the cemented carbides demonstrated the optimal corrosion resistance, with minimum corrosion current density of 4.65 and 0.98 $\mu\text{A}/\text{cm}^2$, respectively. Luo et al^[7] studied the corrosion behavior of WC-high-entropy alloy (HEA) cemented carbide, i.e., WC-10wt% $\text{Al}_x\text{CoCrCuFeNi}$, in 3.5wt% NaCl solution using electrochemical methods. It is found that WC-HEA cemented carbide exhibits significantly superior corrosion resistance than WC-Co. The improved resistance can be attributed to the formation of passive films, specifically Cr_2O_3 and Al_2O_3 , on the surface of the HEA binder. These films effectively inhibit anode dissolution, thereby enhancing the corrosion resistance of the WC-HEA cemented carbides.

Despite its desirable characteristics, WC-Co cemented carbide relies on strategic scarce resources such as tungsten (W) and cobalt (Co). Moreover, Co has the potential to cause various health concerns, such as DNA strand breaks, chromosomal abnormalities, micronucleus formation, or sister chromatid exchanges, making it a potentially carcinogenic substance^[8-9]. Exposure to cobalt dust can lead to “hard metal

disease”, characterized by allergic asthma, respiratory distress, dry cough, intermittent chemical pneumonia (interstitial pneumonia), and pulmonary edema^[10]. Therefore, it is necessary to research alternative wear-resistant materials that do not contain cobalt. To address the limitations of WC-Co cemented carbide in terms of raw material resources and harmful effects of the Co binder on health, this study explored the potential of Ti(C, N)- Mo_2C -Ni cermet as a sustainable alternative to the wear-resistant material. Ti(C, N)-based cermet exhibits excellent mechanical and physicochemical properties, including high hardness, strength, wear resistance^[11], excellent chemical stability, and low cost of raw materials^[12]. Additionally, they demonstrate remarkable resistance to plastic deformation and oxidation^[13]. Compared with WC-Co cemented carbide, Ti(C, N)-based metal ceramics require more abundant raw materials such as titanium (Ti) and nickel (Ni). The global reserve of Ti in the Earth’s crust are approximately 1000 times greater than that of W^[14-15], while the reserve of Ni is 70 times greater than that of Co^[16-17]. By replacing WC-Co cemented carbide with Ti(C, N)-based metal ceramics, strategic scarce resources like W and Co can be conserved, reducing the health risks associated with Co.

In the present study, the electrochemical corrosion and erosion-corrosion behavior of Ti(C, N)-based cermet and WC-Co cemented carbides were compared in alkaline conditions. The corrosion morphology, corrosion rates, microstructure, and volumetric loss rates of the materials in alkaline electrochemical were characterized. The objective is to provide valuable insights for selecting appropriate wear-resistant materials in alkaline conditions.

2 Experiment

2.1 Preparation of materials

In this study, commercially available materials were used for the preparation of Ti(C, N)- Mo_2C -Ni cermet and WC-Co cemented carbides. The raw materials included $\text{TiC}_{0.7}\text{N}_{0.3}$ powder, Mo_2C powder, Ni powder, medium-sized WC powder, fine-sized WC powder, and Co powder. Table 1 provides their particle sizes and chemical composition. The composition of the prepared cermet was denoted as CN16 and designed as $\text{TiC}_{0.7}\text{N}_{0.3}$ -10 Mo_2C -16Ni (wt%). The composition of the prepared cemented carbide was designated as YG6 for the medium-sized WC powder-based material and YG6X for

Table 1 Characteristics of the raw powders

Raw powder	FSSS particle size/ μm	Composition/wt%						
		Total carbon	Free carbon	O	N	Fe	Ni	Cr
$\text{TiC}_{0.7}\text{N}_{0.3}$	3.36	13.29	-	0.54	7.29	0.065	-	-
Mo_2C	1.55	6.03	0.2	0.52	0.15	-	-	-
Ni	2.65	0.1	-	0.1	-	0.005	-	-
WC60	6.44	5.96	0.02	0.02	-	-	-	-
WCR10	1.2	5.95	0.02	0.1	-	0.012	-	0.41
Co	1.10	0.014	-	0.41	-	-	0.0014	-

the fine-sized WC powder-based material, both containing WC-6Co (wt%). The addition of Mo₂C in Ti(C, N)-based metal ceramics aimed to facilitate complete wetting of the ceramic phase Ti(C, N) by the metal binder Ni during sintering. Carbide (or carbonitride) ceramics typically demonstrate superior corrosion resistance and wear resistance than cobalt and nickel metals. To eliminate the factor of difference in ceramic hard phase proportions which affect corrosion resistance performance, the molar proportion of ceramic hard phases TiC_{0.7}N_{0.3} and Mo₂C in Ti(C, N)-based cermet and WC in WC-Co cemented carbides were both set at 82.5%. By doing so, a more accurate representation of the performance of the two materials was achieved in this study.

Both the cermet and the cemented carbides were prepared by powder metallurgy techniques. The mixed powders were ground in a 1 kg stainless steel ball milling tank by a roll ball mill. For CN16, gasoline was used as the grinding medium, and for YG6 and YG6X, anhydrous ethanol was used with a dosage of 300 mL each time. The grinding media consisted of $\Phi 6$ mm WC-6Co alloy balls, with a ball-to-powder ratio of 5:1. The grinding speed was set at 56 r/min, and the grinding time was 72 h for CN16 and fine-sized YG6X, and 48 h for medium-sized YG6. After grinding, the slurry was filtered through a 38 μm sieve and allowed to settle for approximately 12 h. The remaining mixture was then dried in an electric heating vacuum drying cabinet at 90–100 °C for 50–60 min. The resulting powder was mixed with SD rubber binder, dried, and sieved through an 180 μm sieve. The binder ratios were 220 mL/kg for CN16 and 80 mL/kg for YG6 and YG6X. Subsequently, the mixed powders were pressed into green compacts with dimensions of 20 mm \times 6.5 mm \times 5.25 mm, and pre-sintered in a vacuum furnace at 1420 °C for YG6 and YG6X, and 1445 °C for CN16, with a holding time of 1 h. Pressure sintering was then performed under an argon atmosphere with a pressure of 5 MPa. The sintering temperature was 1400 °C and the holding time was 40 min to reduce the porosity of the vacuum-sintered bodies. Table 2 provides the densification, average ceramic phase size, and performance data of the prepared CN16, YG6, and YG6X, where APS represents the average ceramic phase size and TRS represents the transverse rupture strength.

2.2 Electrochemical corrosion and erosion-corrosion

Electrochemical corrosion tests were conducted on a CS4 three-electrode electrochemical workstation. The auxiliary electrode was Ag/AgCl, and the corrosion solution was a 5wt% NaOH solution. The dynamic potential scanning technique was employed with a scanning range from -2.0 V to 1.5 V, scanning rate of 2 mV/s, frequency of 2.00 Hz, and

Table 2 Properties of CN16, YG6, and YG6X

Material	APS/ μm	Density/ $\text{g}\cdot\text{cm}^{-3}$	TRS/MPa	Hardness/HRA
CN16	0.9	5.68	1714	92.8
YG6	1.4	14.95	1763	91.8
YG6X	0.7	14.85	2185	93.2

scanning time of 1500 s, at an experimental temperature of 25 °C. Fig. 1 presents a schematic diagram of the erosion-corrosion setup. Prior to eroding, the surface areas of all samples were measured to ensure uniformity. During eroding, the samples were affixed to a stirring blade rotating at 550 r/min, with an eroding time of 120 min. Eroding media included alkaline solution (5wt% NaOH), sand-water mixture (5wt% SiO₂), and alkaline sand-water mixture (5wt% SiO₂+5wt% NaOH). The sand particles had a size of 180–250 μm and a hardness of 900–1200 HV.

Surface morphologies of the electrochemical corrosion and erosion-corrosion were examined using a Hitachi S-4800 high-resolution field emission scanning electron microscope (SEM) with secondary electron imaging. The surface composition was analyzed by energy dispersive spectrometer (EDS) attached to the SEM. In this study, the eroding corrosion evaluation focused on the volume loss rate to eliminate the density factor, which is significant because the density of CN16 is less than half of that of YG6 and YG6X. The volume loss rate was calculated by the following formula:

$$v = \frac{\Delta m}{\rho t} \quad (1)$$

where the erosion-corrosion rate is represented as v (mm³/h); mass loss is represented as Δm (mg); density is represented as ρ (g/cm³); erosion-corrosion time is denoted as t (h). Five samples of each grade material, with dimension of 5 mm \times 5 mm \times 5 mm, underwent surface grinding and polishing to obtain 1 μm surface finish through diamond paste. The initial mass of the samples was measured by a precision electron balance (model BSA124S) with an error of 0.1 mg before the erosion-corrosion tests. Following the tests, the samples were removed from the impellers, cleaned with acetone using an ultrasonic bath for 10 min to eliminate residual slurry, and subsequently dried. The mass of each sample was recorded to determine mass loss. These procedures were repeated for each grade, and the average results of the five samples were used to determine the mass loss for each grade material. The erosion-corrosion rate was determined by the average value of the volume loss rate.

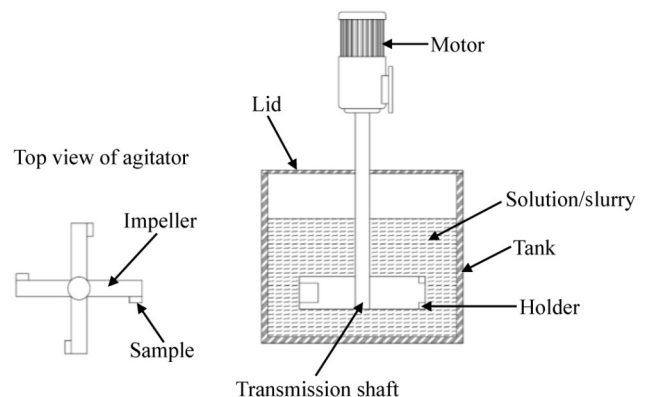


Fig.1 Schematic of the device for erosion-corrosion

3 Results and Discussion

3.1 Alkaline electrochemical corrosion of cermet and cemented carbides

Fig. 2 illustrates the surface morphologies of the cermet CN16, medium-grain cemented carbide YG6, and fine-grain cemented carbide YG6X before and after electrochemical corrosion in alkaline solution. After corrosion, the surface becomes rough and uneven compared to its initial smooth state. The metal binder phase region demonstrates lesser corrosion resistance than the surrounding ceramic hard phase region. Under alkaline electrochemical corrosion conditions, CN16 and YG6 surfaces retain some white binder phase, while YG6X surface shows almost complete corrosion of the binder phase, indicating inferior electrochemical corrosion resistance of YG6X. In Fig. 2b, numerous grooves are visible on the CN16 surface after electrochemical corrosion, resulting from the corrosion of the Ni binder phase. Among Ti(C, N)-based cermet, the corrosion resistance of the metallic component Ni is significantly lower than that of the ceramic

components Ti(C, N) and Mo₂C.

Fig. 3 displays the X-ray diffraction (XRD) patterns of the surfaces of the cermet CN16 and the cemented carbides YG6 and YG6X after electrochemical corrosion. Ti(C, N) is the primary component of CN16 in Fig. 3a, known for its high corrosion resistance. The XRD pattern reveals the structural integrity of Ti(C, N) during corrosion. (Mo, Ti)(C, N) forms as a corrosion-resistant solid solution of Mo₂C and Ti(C, N) during sintering. The corrosion process leads to the formation of titanium oxide (TiO₂). In alkaline conditions, Ti(C, N) reacts with water and oxygen to produce TiO₂. Presence of Ni and Ni₂O₂(OH) indicates the oxidation of binder phase Ni during corrosion, forming Ni₂O₂(OH) with hydroxide ions in NaOH solution. The diverse phases in the Ti(C, N)-based cermet exhibit varying reaction rates and mechanisms during corrosion. In electrochemical corrosion, the binder phase Ni acts as the anode, undergoing oxidation and electron releasing, while the ceramic phase Ti(C, N) and (Mo, Ti)(C, N) function as the cathode, accepting electrons. Ni is prone to preferential corrosion due to its lower potential, while Ti(C, N) and

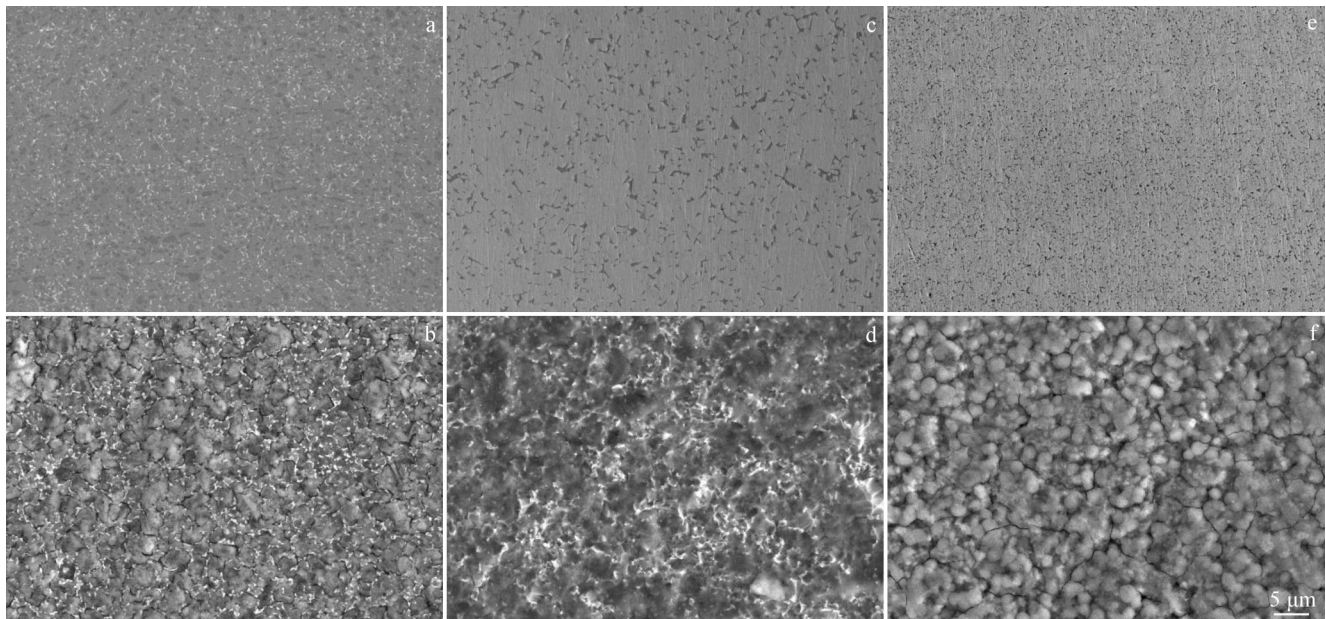


Fig.2 Surface morphologies of materials before (a, c, e) and after (b, d, f) electrochemical corrosion in alkaline solution: (a–b) CN16; (c–d) YG6; (e–f) YG6X

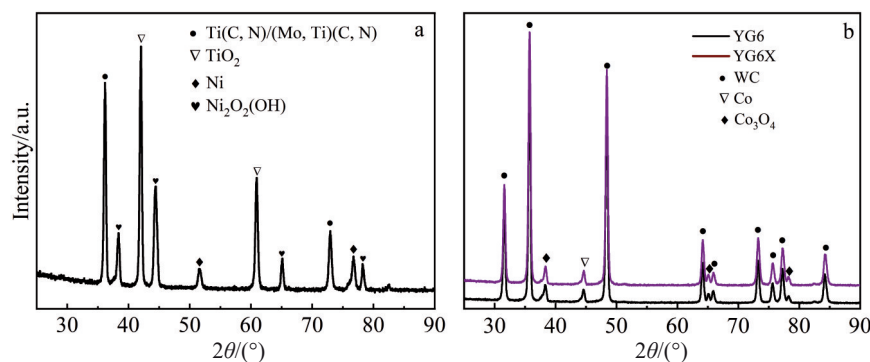


Fig.3 XRD patterns of surfaces after electrochemical corrosion: (a) CN16, (b) YG6, and YG6X

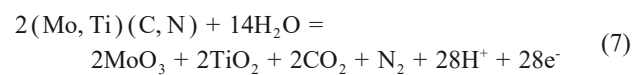
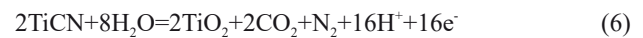
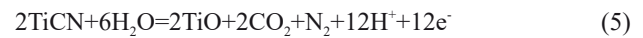
(Mo, Ti)(C, N) demonstrate strong corrosion resistance due to their higher chemical stability. In alkaline conditions, the surface of the Ti(C, N)-based cermet undergoes oxidation, resulting in oxide like TiO_2 .

The primary hard phase in cemented carbides is WC, which exhibits sharp diffraction peaks in the XRD pattern of Fig.3b. Due to its high chemical stability, WC remains relatively stable during corrosion. In contrast, the Co binder is more susceptible to corrosion in NaOH solutions. The XRD analysis results reveal a notable weakening of the Co diffraction peaks and the disappearance of some crystal face peaks, indicating consumption of the Co phase during corrosion. In alkaline environment, Co oxidizes to form the metal oxide Co_3O_4 , which is evident from new diffraction peaks in the XRD pattern. The corrosion products of YG6 and YG6X are similar. Notably, the fine-sized WC powder used in YG6X enhances surface area, resulting in a more dispersed and thinner distribution of the Co phase. This increased contact area accelerates corrosion rates, reflected by more prominent Co_3O_4 diffraction peaks in the XRD pattern. During electrochemical corrosion, the Co phase, acting as the anode material, is more prone to electron loss and oxidation. The chemical interaction between the NaOH solution and Co further promotes Co dissolution.

Fig. 4 presents the surface composition analysis of the cermet CN16, medium-grain cemented carbide YG6, and fine-grain cemented carbide YG6X after electrochemical corrosion in alkaline solution. The composition of CN16's corroded surface reveals a significant increase in oxygen content, which can be attributed to the formation of corrosion products during electrochemical corrosion in the alkaline solution. At 298 K, the electrode potential $E_{\text{Ni}^{2+}/\text{Ni}}$ is -0.257 V. This potential allows Ni to react with the NaOH solution through the following reaction equations^[18]:



When the metal binder Ni is corroded, the enclosed ceramic hard phase becomes exposed to the corrosive solution, leading to corrosion of the ceramic hard phase. In an alkaline electrochemical corrosion solution, the ceramic hard phase Ti(C, N) undergoes corrosion and oxidation, resulting in the formation of TiCNO, TiO, or TiO_2 . Moreover, the introduced Mo_2C , which is dissolved in Ti(C, N), is also corroded and oxidized. The reaction equations^[19-21] are as follows:



The dissolution of the reaction product MoO_3 in the corrosive solution leads to a decrease in corrosion resistance^[22]. Furthermore, upon examining the microstructure and surface composition of YG6 and YG6X after corrosion, it is evident that their surfaces are covered with corrosion products, which prominently contain oxygen. This oxygen primarily originates from the corrosive NaOH solution. Considering the electrode potential, Co behaves as a moderately active metal and shares similarities with amphoteric metals, making it susceptible to corrosion by NaOH. The reaction equations^[23-24] are as follows:



Fig. 5 displays the potentiodynamic polarization curves of CN16, YG6, and YG6X in alkaline solution. The graph depicts two sections: the cathodic polarization section ranging from -2.0 V to -1.25 V, and the anodic polarization section spanning from -1.25 V to 1.5 V. Notably, as the potential increases gradually from -1.25 V to 0 V, the corrosion current

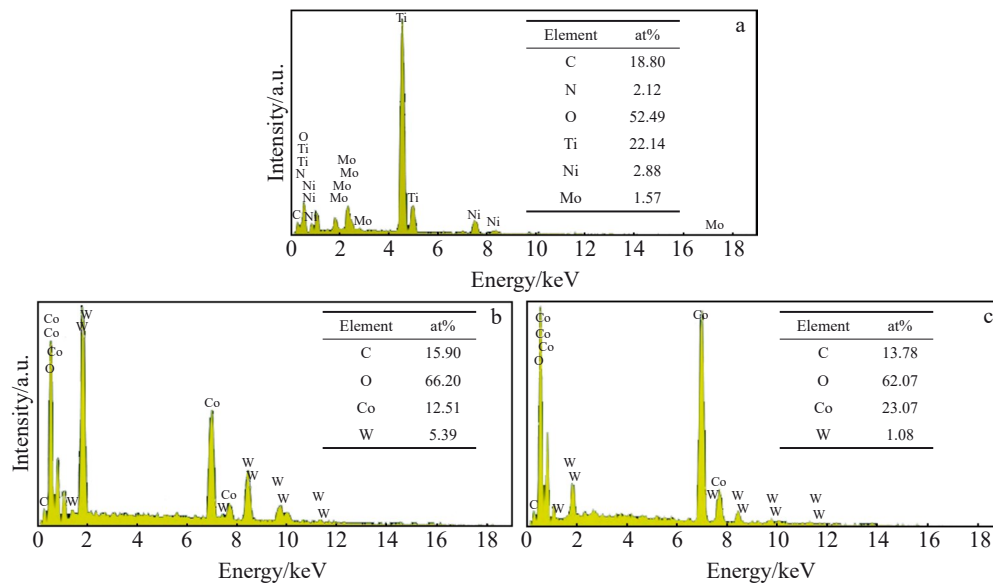


Fig.4 EDS results of surface composition of materials after electrochemical corrosion in alkaline solution: (a) CN16; (b) YG6; (c) YG6X

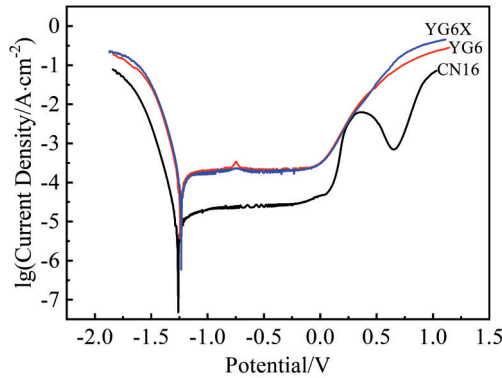


Fig.5 Polarization curves of electrochemical corrosion in alkaline solution

density of YG6 and YG6X remains stable. However, upon further increase in potential from 0 V to 0.5 V, the corrosion current density of YG6 and YG6X shows a continuous rise without any observable passivation region. This suggests that no significant passivation film forms during the corrosion process.

CN16 exhibits a typical passivation phenomenon during electrochemical corrosion in alkaline solution. As the potential increases from 0 V, the current density also increases. Once the potential reaches its peak value, the current density rapidly decreases. This decrease occurs due to the formation of a high-resistance passivation film on the surface of CN16, which improves its corrosion resistance^[25-26]. This passivation film isolates the material from the corrosive solution, effectively protecting the material and reducing the corrosion rate. The polarization curve of CN16 clearly demonstrates the existence of a passivation region, where the current density increases to reach the peak and then decreases. Since CN16 is a composite material consisting of metal Ni, ceramic Ti(C, N), and Mo₂C, the overall electrochemical corrosion polarization curve of CN16 represents the combined behavior of each constituent material. Each peak and valley in the curve correspond to the corrosion behavior of a specific constituent material. Comparing the polarization curve of CN16 with that of pure Ni, it is evident that the passivation region in the CN16 curve corresponds to the passivation of the metal binder Ni^[27]. Consequently, the process of corrosion current density increasing to the peak and then decreasing corresponds to the stage where the metal binder Ni starts to corrode and subsequently reacts to form a passivation film, preventing further corrosion. After reaching the lowest point of the current density, the potential continues to rise, causing the current density to increase steadily. Overall, when the corrosion potential changes from -1.25 V to 0 V, the corrosion

current density of CN16 remains stable. However, as the corrosion potential changes from 0 V to 0.5 V, the corrosion current density rapidly increases to a peak, then rapidly decreases, and finally increases steadily after reaching the lowest point. The relevant parameters of the potentiodynamic polarization curves for CN16, YG6, and YG6X in alkaline solution are summarized in Table 3. According to the electrochemical polarization curves, the corrosion potential (E_{corr}) and corrosion current density (I_{corr}) of the materials can be determined. The corrosion current density can be obtained by the Stern-Geary equation^[28].

$$I_{\text{corr}} = \frac{b_a b_c}{2.303(b_a + b_c)} \cdot \frac{1}{R_p} \quad (11)$$

where the slopes of the cathodic and anodic polarization curves, referred to as Tafel slopes, are represented by b_c and b_a , respectively, measured in mV/dec; additionally, the polarization resistance is represented by R_p , measured in $\text{k}\Omega \cdot \text{cm}^2$. R_p can be calculated by Eq.(12).

$$R_p = \left(\frac{\Delta E}{\Delta i} \right) \Big|_{\Delta E \rightarrow 0} \quad (12)$$

where ΔE represents the polarization potential, and Δi represents the polarization current. It is evident that under similar potential conditions, the corrosion current decreases as the impedance increases. This relationship is supported by Eq. (11), which highlights that a higher impedance R_p corresponds to a smaller corrosion current density, indicating better corrosion resistance of the material. Table 3 demonstrates that the impedance R_p of CN16 is approximately one order of magnitude higher than that of YG6 and YG6X. Consequently, the corrosion rate of CN16 is the lowest, approximately one-tenth of that of YG6 or YG6X. It is worth noting that the structure and composition of materials can significantly influence their corrosion performance^[29]. In CN16, the metal binder is Ni, whereas in YG6 and YG6X, the metal binder is Co. It is known that at 298 K, the electrode potential $E_{\text{Ni}^{2+}/\text{Ni}}$ is -0.257 V, while $E_{\text{Co}^{2+}/\text{Co}}$ is -0.28 V, indicating that metal Co is more susceptible to reaction and corrosion. This change in the composition of the metal binder significantly improves the corrosion resistance of CN16.

3.2 Erosion-corrosion and erosive wear of cermet and cemented carbides

3.2.1 Erosion-corrosion by alkaline solution

The surface morphologies of materials before erosion-corrosion are shown in Fig. 6. Before erosion-corrosion, the surface of Ti(C, N)-based cermet CN16 displays a distinctive core-rim-binder structure. The dark core consists of the Ti(C, N) phase, while the grey rim phase is an intricate solid solution of Mo₂C dissolved in Ti(C, N)^[30], with the binder phase arranged in a strip-like manner surrounding the hard

Table 3 Parameters of the polarization curves for different materials in NaOH solution

Material	R value	$b_a/\text{mV} \cdot \text{dec}^{-1}$	$b_c/\text{mV} \cdot \text{dec}^{-1}$	E_{corr}/V	$R_p/\Omega \cdot \text{cm}^2$	$I_{\text{corr}}/\text{mA} \cdot \text{cm}^{-2}$	Corrosion rate/ $\text{mm} \cdot \text{a}^{-1}$
CN16	0.98	142.13	54.51	-1.2607	2601.9	0.0054	0.0328
YG6	0.99	122.98	57.97	-1.2407	264.14	0.0629	0.4054
YG6X	1.00	129.18	56.69	-1.233	216.95	0.0657	0.4262

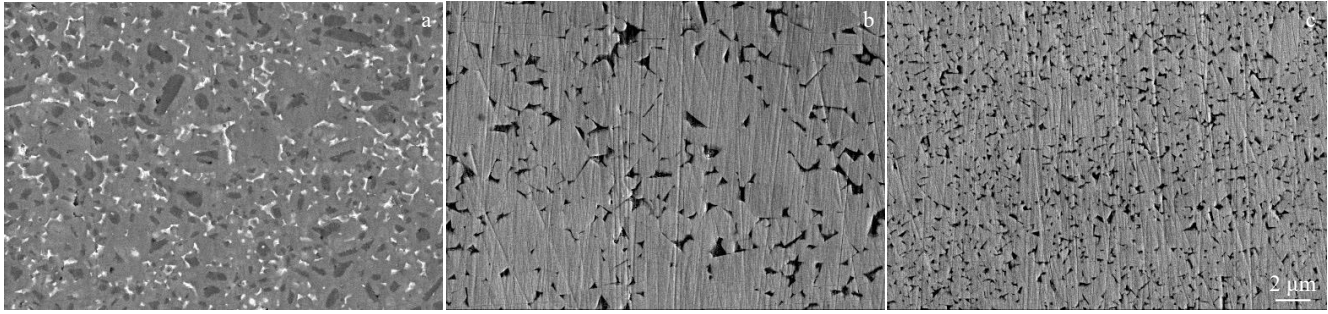


Fig.6 Surface morphologies of materials before erosion-corrosion: (a) CN16; (b) YG6; (c) YG6X

phase. This multi-phase structure enhances overall performance by providing hardness from the hard phase and toughness through the binder phase. Cemented carbide is primarily made up of the hard phase WC and the Co-based binder phase. On a microscopic level, the WC phase typically forms irregular quadrilateral or triangular structures, with the binder phase interspersed between them. Comparatively, the edges of the hard phase in the Ti(C, N)-based cermet are smoother, whereas that in the cemented carbide is sharper, impacting their impact wear resistance. Fig.6b and 6c reveal the microstructures of cemented carbides YG6 and YG6X, respectively. YG6X, whose hard phase size is smaller than that of YG6, generally exhibits higher hardness and better wear resistance due to the increased hard phase contact points afforded by the smaller particles. The multi-phase structure of the Ti(C, N)-based cermet may aid in stress dispersion during erosion-corrosion, thereby increasing its wear resistance.

Additionally, the particle size of the hard phase in the cemented carbides directly influences its wear resistance and fracture toughness.

Fig. 7a displays the volumetric loss rates of cermet CN16, cemented carbides YG6 and YG6X under dynamic alkaline solution corrosion. It is observed that as the corrosion time increases, the volumetric loss rate of the materials consistently decreases. The primary cause of volumetric loss during the surface flushing with the alkaline solution is the corrosion of the metal binding phase. Initially, the metal binding phase on the material surface is fully exposed to the corrosive solution, resulting in a large contact area and a fast corrosion rate, and leading to a relatively high volumetric loss rate. However, over time, the metal binder phase on the material surface gradually is corroded. Consequently, the corrosion pits are deepened, and their contact area with the corrosive solution decreases, causing a gradual reduction in the corrosion rate.

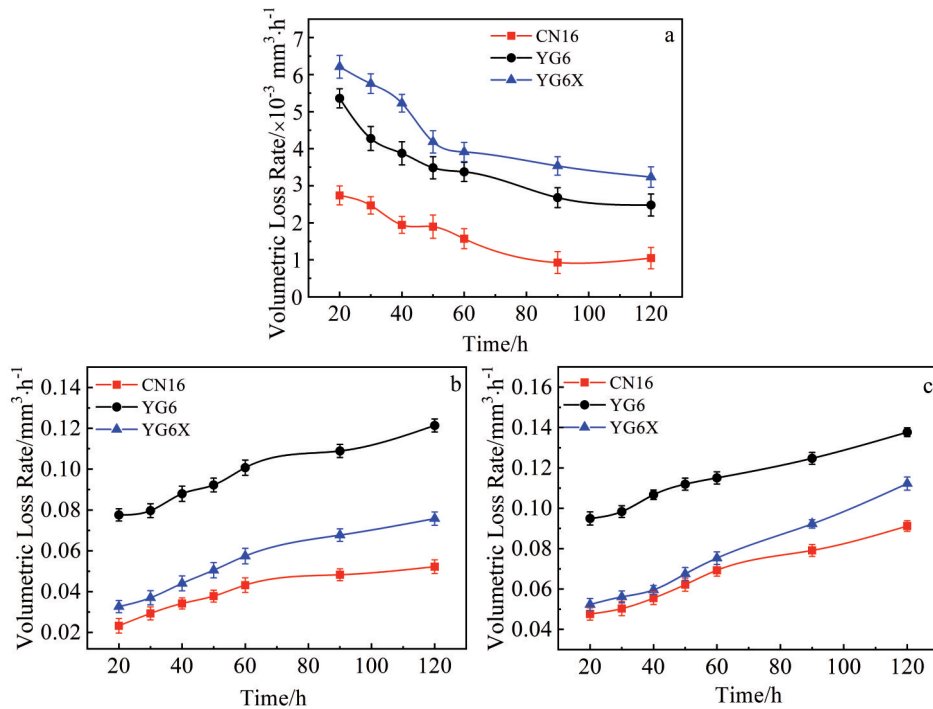


Fig.7 Erosion-corrosion rate of CN16, YG6, and YG6X in different conditions: (a) alkaline solution; (b) sand-water mixture; (c) alkaline sand-water mixture

In dynamic corrosion with rapid flow of alkaline solution, corrosion products adhere to the corroded surface, creating a temporary barrier that prevents further contact between the solution and the material's fresh surface, thereby inhibiting corrosion. However, as the alkaline solution erodes the surface, dissolved corrosion products mix with the solution, allowing unrestricted direct contact and ongoing corrosion of the fresh surface. Fig. 8 depicts the surface morphologies of CN16, YG6, and YG6X after eroding in the alkaline solution for 120 min. The binder phases experience corrosion while the hard phases remain almost unaffected. Comparing the corrosion characteristics, the metal binder phase of YG6 and YG6X undergoes more severe corrosion, resulting in deeper pits, whereas the binder phase of CN16 displays shallower pits. Considering that both Ni and Co have comparable densities of 8.9 g/cm^3 , the volumetric loss rate of CN16 is lower than that of YG6 and YG6X. Specifically, YG6X demonstrates a higher volumetric loss rate than YG6. This can be attributed to the smaller average size of the ceramic phase in YG6X, which exposes more dispersed metal binder phases on the material surface. Consequently, the contact area with the alkaline solution is larger, resulting in faster corrosion rate. Additionally, the improved corrosion resistance of the Ni binder in CN16, compared with the Co binder in YG6 and YG6X, contributes to the slowest corrosion rate of CN16.

3.2.2 Erosive wear by sand-water mixture

Fig. 7b displays the volumetric loss rates of cermet CN16 as well as cemented carbides YG6 and YG6X after abrasive erosion in sand-water mixture. The graph demonstrates an increase in volumetric loss rates as the erosion time

progresses. Initially, the material surfaces are relatively smooth, resulting in fewer pits caused by sand particles, and leading to smaller volumetric loss rate. However, with prolonging the erosion time and increasing number of sand particles, the number of pits on the surface continues to rise. These pits are more susceptible to cracking due to the impact of sand particles, eventually leading to gradual fragmentation and detachment, and thus increasing the volumetric loss rate. Among the materials studied, YG6 exhibits the highest volumetric loss rate. The rotational linear speed was 5.76 m/s , resulting in high-speed relative erosion between the materials and the sand particles. Under such conditions, the resistance to abrasive particle wear plays a crucial role in mitigating material loss, and this resistance is closely linked to the material's hardness. Generally, materials with higher hardness exhibit better resistance to abrasive particle wear. CN16 has a hardness of 92.8 HRA, YG6 has a hardness of 90.5 HRA, and YG6X has a hardness of 92.9 HRA. From a hardness perspective, YG6 has lower hardness than CN16 and YG6X, resulting in the highest volumetric loss rate.

It also indicates that CN16 demonstrates the lowest volumetric loss rate. The resistance to abrasive particle wear is determined not only by hardness but also microstructure. Fig. 9 illustrates the surface morphologies of CN16, YG6, and YG6X after of erosion in sand-water mixture for 120 min. CN16 exhibits ceramic hard phase with core phase and surrounding rim phase, resulting in the rounded or elliptical shapes of the ceramic hard phase's edges (Fig. 9a). This configuration weakens stress concentration at the edges and impedes cracking, fracturing, and delamination upon impact by sand particles. In contrast, the WC ceramic hard phase in

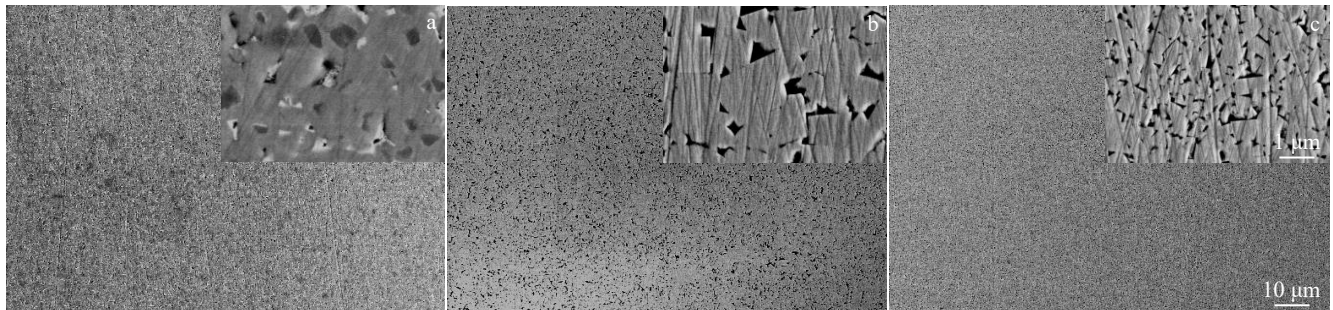


Fig. 8 Surface morphologies of CN16 (a), YG6 (b), and YG6X (c) after dynamic alkaline solution corrosion for 120 min

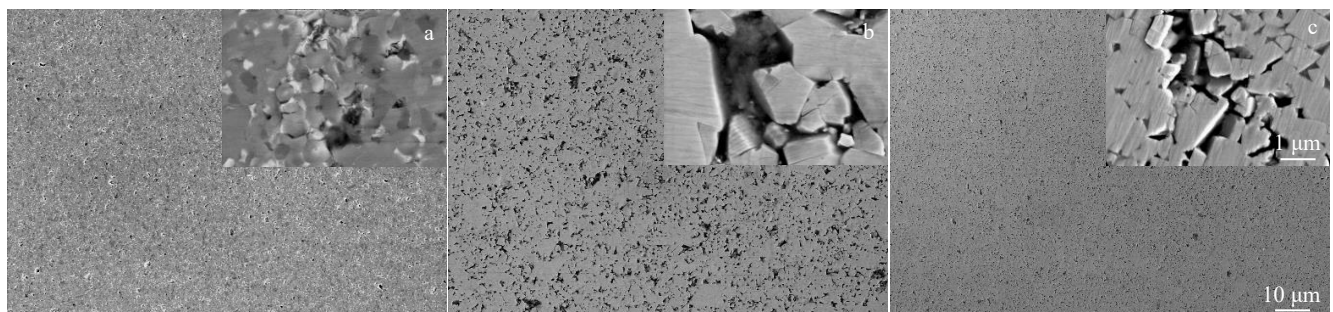


Fig. 9 Surface morphologies of CN16 (a), YG6 (b), and YG6X (c) after erosion by sand-water mixture for 120 min

YG6X appears irregular with sharp edges and corners (Fig.9c). These irregularities and sharp edges promote stress concentration upon impact, leading to cracking, fracturing, and subsequent detachment. Consequently, despite YG6X having a slightly higher hardness than CN16, its volumetric loss rate is greater. Additionally, compared to the alkaline solution corroding discussed earlier, the erosive action of the sand-water mixture results in a volumetric loss rate that is one order of magnitude higher, indicating a more significant damaging effect of sand particle erosion.

3.2.3 Alkaline erosion-corrosion of cermet and cemented carbides

Fig.7c presents the volumetric loss rates of cermet CN16 as well as cemented carbides YG6 and YG6X when exposed to alkaline sand-water mixture. As the erosion-corrosion time increases, the volumetric loss rates of the materials gradually rise. The metal binder phase undergoes corrosion and dissolution into the mixture, while the ceramic hard phase experiences fragmentation and delamination, resulting in volumetric loss for both the metal ceramic and cemented carbide. During the erosion-corrosion process, there is a reaction between SiO_2 and NaOH . However, the reaction rate is slow, and the resulting Na_2SiO_3 product does not significantly impact the process. Thus, the influence of this reaction on the erosion-corrosion can be negligible. The reaction equation is as follows^[31]:



The metal binder phase in both the cermet and cemented carbides reacts with NaOH , resulting in the formation of corrosive oxidation products. These corrosion products initially cover the original surface and are subjected to intense erosion from the sand-water mixture. However, the adhesion between the corrosion products and the substrate is weak, leading to easy washout before completely covering the original surface. Consequently, they dissolve into the sand-water mixture. Moreover, the reaction between the metal binder phase and NaOH proceeds slowly. As a result, corrosion products exhibit restricted ability to inhibit the erosive wear and corrosion of the alkaline sand-water mixture. The removal of corrosion products signifies a loss of the binder phase, which contributes to the volumetric loss in both the cermet and cemented carbides.

Another factor contributing to surface damage and volumetric loss in cermet and cemented carbides is the delamination of the ceramic hard phase. In the erosion process, as abrasive sand particles impact the surface of materials, the high-speed impact forces vary in their probability of hitting the metal binder phase. Consequently, the metal binder phase experiences uneven stress, which leads to varying rates of chemical reactions. The regions experiencing higher stress are preferentially corroded, resulting in the expansion of the corrosion region. Upon destruction of the metal binder phase, corrosion pits form, intensifying the damage to the edges of the ceramic hard phase caused by abrasive sand particles. Moreover, the

presence of corrosion pits increases the contact surface area between the material and the alkaline mixture, thus accelerating the corrosion process. As the abrasive sand particles impact and shatter the edges of the ceramic hard phase, the fragmented pieces are subsequently carried away by the running mixture, leading to volumetric loss of the material.

In the conditions of erosive and corrosive alkaline sand-water mixture, the metal binder phase plays a crucial role in preserving and delaying the destruction of the ceramic hard phase. The damage to cermet and cemented carbides primarily originates from the metal binder phase. Due to the significant difference in corrosion resistance between the metal binder phase and the ceramic hard phase, the metal binder phase firstly undergoes corrosion. Afterwards, the ceramic hard phase, enclosed by the metal binder phase, is directly exposed to the erosive mixture, and the surface exposure of the ceramic hard phase is increased in the eroding. Given the lower toughness of the ceramic hard phase, the exposed surfaces are vulnerable to crack formation and fragmentation upon impact by abrasive sand particles. Following the corrosion of the metal binder phase, the ceramic hard phase particles, previously bonded and supported by the metal binder phase, is detached^[32]. Smaller particles are particularly prone to detachment than larger particles^[33-35]. Consequently, the detachment of ceramic hard phase particles gives rise to concave pits that proliferate through the combined effects of corrosion and erosion. As a result, the erosive and corrosive process in cermet and cemented carbides intensifies over time, leading to an accelerated volumetric loss rate.

YG6 exhibits the highest rate of volumetric loss under the erosive-corrosive action of alkaline sand-water mixture, indicating its weakest resistance to erosion-corrosion. Although YG6 demonstrates better resistance to dynamic corrosion in alkaline solutions than YG6X, it shows notably weaker performance in resisting abrasion caused by sand-water mixture erosion than YG6X. Fig. 10 illustrates the surface morphologies of CN16, YG6, and YG6X after erosion-corrosion in the alkaline sand-water mixture for 120 min. It is evident that the corrosion effect is relatively weak, and the material damage is primarily attributed to erosive impact wear, and the non-impacted regions remain smooth. In other words, during the erosive-corrosive process of the alkaline sand-water mixture, the primary mechanism of material loss is the impact abrasion of sand particles, with minimal corrosive effect. Consequently, YG6 experiences a higher volumetric loss rate. Additionally, since impact abrasive wear is dominated by sand particles, the trend in volumetric loss rate for CN16, YG6, and YG6X under the erosive-corrosive action of the alkaline sand-water mixture is similar to that in the case of the simple sand-water mixture. CN16 exhibits superior resistance to impact abrasion caused by the sand-water mixture than YG6X, and its resistance to dynamic corrosion by alkaline solutions is also better than that of YG6X. Therefore, CN16 performs better in overall resistance to erosion-corrosion in the alkaline sand-water mixture.

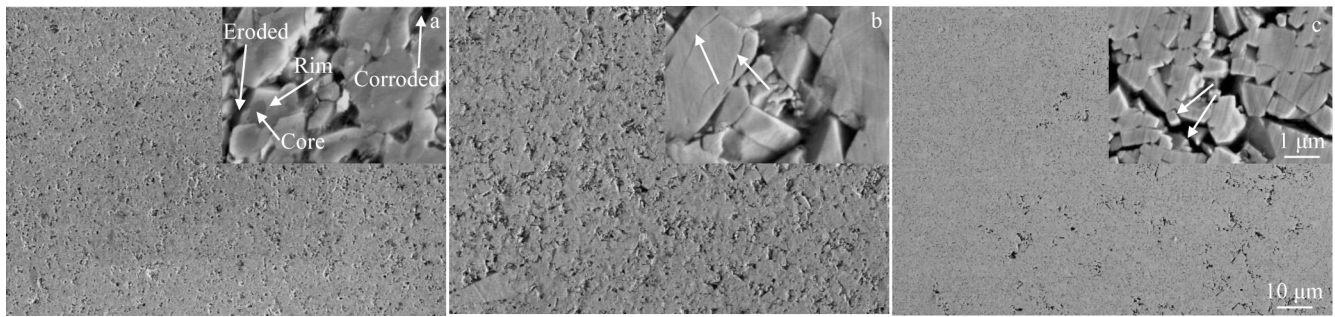


Fig.10 Surface morphologies of CN16 (a), YG6 (b), and YG6X (c) after erosion-corrosion by alkaline sand-water mixture

The surface of CN16 shows simultaneous traces of corrosion and erosion due to abrasive particle impact, as depicted in Fig. 10a. Corrosion is mainly observed in the region of the metal binder phase, resulting in a rough surface and accumulation of corrosion products in the pits. Conversely, the ceramic hard phase experiences fracturing and detachment due to abrasive particle impact, leading to a smoother interface. The ceramic hard phase in the microstructure of CN16 has a core-rim structure. This rim phase, which is inherently brittle^[36], tends to initiate and propagate cracks when subjected to the impact and erosion of abrasive particles. Consequently, the rim phase is more susceptible to fracture, while the core phase remains relatively intact, with cracks not crossing directly through it. In YG6, the ceramic hard phase has a larger average size, which increases the likelihood of internal structural defects within the larger tungsten carbide grains. As a result, YG6 exhibits more cracks, and transgranular fracture modes are more prevalent, as depicted by the arrows in Fig. 10b. YG6X has a smaller average size of ceramic hard phase with a greater number of phase boundaries. The well-developed small WC grains in YG6X possess higher strength, so the bonding strength between the ceramic hard phase and the metal binder phase is lower than the strength of ceramic hard phase itself. Consequently, cracks tend to propagate along the phase boundaries during crack extension, as indicated by the arrows in Fig. 10c.

3.3 Comparison of material loss under different erosion conditions

By comparing material loss under various conditions such as dynamic alkaline solution corrosion, sand-water mixture abrasion, and erosion-corrosion by alkaline sand-water mixture, several conclusions can be made. When subjected to simple alkaline solution erosion (Fig. 8), both the cermet and cemented carbide surfaces display numerous corrosion pits. In the alkaline solution, the metal binder phase on surfaces reacts with NaOH, leading to the corrosion of the metal binder phase. The NaOH solution flows over the surface of the cermet and cemented carbides at a specific velocity, resulting in a more rapid removal and dissolution of the exposed metal binder phase. As there is no impact from sand particles, the ceramic hard phase is less prone to detachment. Therefore, the effect of alkaline solution erosion essentially expedites the

corrosion process.

From the morphology of erosion by sand-water mixture (Fig. 9), it is evident that the cermet and cemented carbide surfaces undergo deformation due to the impact of sand particles, which leads to particle loosening, displacement, and uneven surface. The presence of small broken particles can also be observed. Importantly, these deformed and broken particles detach from the material surface during erosion, forming pits. Comparatively, the destructive effect of sand particle erosion is more severe than that of alkaline erosion-corrosion within the same-time frame. Despite partial erosion of the metal binder phase, remnants of the metal binder phase still exist on the surface of the cermet and cemented carbides. Sand-water mixture erosion primarily involves the impact and wear down of the material surface by sand particles, while the mixture flushes away and removes the resulting debris.

Fig. 10 clearly demonstrates that when corrosion by the corrosive solution and erosion by sand particles occur simultaneously, the metal binder phase on the surface of the cermet and cemented carbides undergoes corrosion, causing the ceramic hard phase particles unsupported. The impact of sand particles and the action of the dynamic solution dislodges these ceramic hard phase particles, resulting in the formation of numerous pits. As these pits expose fresh surfaces, the metal binder phase will be further corroded, and the ceramic hard phase particles continue to detach due to the impact of sand particles and the flushing action of the mixture. Consequently, the pits become deeper. After the combined action of erosion and corrosion, the surface of the cermet and cemented carbides comprises the remaining original ceramic hard phases, a small number of metal binder phases, and newly formed pits. It is worth noting that the effect of alkaline sand-water mixture erosion is not merely the combination of the corrosion effect of the corrosive solution and the erosion effect of the sand-water mixture. Instead, it involves mutual interaction and promotion of both corrosion and erosion, leading to an accelerated destructive process.

4 Conclusions

1) When exposed to alkaline solutions, the cermet exhibits passivation, which leads to a significant increase in oxygen content on the corroded surface. The fine-grained cemented carbides have higher corrosion rate, followed by the medium-

grained cemented carbides. Notably, the corrosion rate of the cermet is approximately one order of magnitude lower than that of cemented carbides.

2) In the alkaline sand-water mixture, both the cermet and cemented carbides experience an increase in volume loss rate over time. The medium-grained cemented carbide exhibits the highest volume loss rate, followed by the fine-grained one. The cermet demonstrates the lowest volume loss rate. During the impacts by sand particles, cracks tend to penetrate the rim phase of the cermet, while the core phase remains relatively intact. In contrast, transgranular fracture is more common in medium-grained cemented carbides, and cracks tend to propagate along grain boundaries in fine-grained cemented carbides.

3) The abrasive effect of sand particles is the primary reason for degradation in the erosion-corrosion process of alkaline sand-water mixture. This process is not simply the combination of individual alkaline solution corrosion and sand-water mixture erosive wear. Instead, it involves mutual interaction and promotion of both erosive corrosion and wear, leading to an accelerated destructive process.

References

- Sathya K, Nagarajan K, Carlin Geor Malar G et al. *Applied Water Science*[J], 2022, 12(4): 70
- Yuan X K, Zhang X H, Deng S X. *Rare Metal Materials and Engineering*[J], 2019, 48(8): 2454
- Li Meng, Gong Manfeng, Cheng Zanlin et al. *Rare Metal Materials and Engineering*[J], 2023, 52(7): 2653 (in Chinese)
- Yang Y L, Chen J H, Lu H et al. *Rare Metal Materials and Engineering*[J], 2023, 52(5): 1774
- Tang T T, Xiao X L, Xu K et al. *International Journal of Refractory Metals and Hard Materials*[J], 2023, 110: 106044
- Li H J, Zhang S F, Ouyang S L et al. *International Journal of Refractory Metals and Hard Materials*[J], 2023, 117: 106408
- Luo W Y, Liu Y Z, Dong B W et al. *Intermetallics*[J], 2022, 151: 107738
- Simonsen LO, Harbak H, Bennekou P. *Science of Total Environment*[J], 2012, 432: 210
- Karagas M R, Wang A, Dorman D C et al. *Lancet Oncology*[J], 2022, 23(5): 577
- Nemery B, Verbeken E K, Demedts M. *Seminars in Respiratory and Critical Care Medicine*[J], 2001, 22(4): 435
- Liu A J, Liu N. *Rare Metal Materials and Engineering*[J], 2019, 48(2): 375
- Xiang Z N, Li Z J, Huang S G et al. *Rare Metal Materials and Engineering*[J], 2021, 50(4):1179
- Yang Qingqing, Xiong Weihao, Huang Bin et al. *Rare Metal Materials and Engineering*[J], 2022, 51(11): 4166 (in Chinese)
- Harald Ulrik S, Antony Elias S. *Sustainable Horizons*[J], 2023, 7: 100067
- Wang X, Qin W Q, Jiao F et al. *Transactions of Nonferrous Metals Society of China*[J], 2022, 32(7): 2318
- Yu Z, Wang Y L, Ma X Q et al. *Resources Policy*[J], 2023, 85: 103861
- Wang Y W, Chang X J, Chen M J et al. *Minerals Engineering*[J], 2023, 203: 108336
- Liang M X, Wan W C, Guo Z X et al. *International Journal of Refractory Metals and Hard Materials*[J], 2014, 43: 322
- Wan W C, Xiong J, Yang M et al. *International Journal of Refractory Metals and Hard Materials*[J], 2012, 31(2): 179
- Lavrenko Vladimir A, Panasyuk A D, Martine D B et al. *Journal of European Ceramic Society*[J], 2005, 25: 1813
- Lavrenko V A, Shvets V A, Umanskii A P et al. *Powder Metallurgy and Metal Ceramics*[J], 2004, 43: 62
- Yong C, Baik N I, Lee J S et al. *Composites Science and Technology*[J], 2001,61: 981
- Neville A, Hu X. *Wear*[J], 2001, 251: 1284
- Guo Z X, Xiong J, Wan W C et al. *International Journal of Applied Ceramic Technology*[J], 2014 11: 1045
- Bolognini S. *International Journal of Refractory Metals and Hard Materials*[J], 2003, 21: 19
- Lee J Y, Kim J H, Lee H M. *Journal of Alloys and Compounds*[J], 2000, 297: 231
- Manoj Kumar B V, Balasubramaniam R, Bikramjit B. *Journal of the American Ceramic Society*[J], 2007, 90(1): 205
- William Grips V K, Barshilia Harish C. *Thin Solid Films*[J], 2006, 514: 204
- Zhang D W, Zhang X P. *Surface & Coating Technology*[J], 2005, 190(2-3): 212
- Qiu H, Li X, Pan C et al. *Materials*[J], 2023, 16(16): 5645
- Liu Y, Lin Q, Chen J et al. *Colloids and Surfaces A: Physicochemical and Engineering Aspects*[J], 2022, 648: 129279
- Gee M G, Gant A, Roebuck B. *Wear*[J], 2007, 263: 137
- Cardinal S, Malchère A, Garnier V et al. *International Journal of Refractory Metals and Hard Materials*[J], 2009, 27: 521
- Liu N, Shi M, Xu Y D et al. *International Journal of Refractory Metals and Hard Materials*[J], 2004, 22: 265
- Hussainova I. *Wear*[J], 2003, 255: 121
- Ostberg G, Buss K, Christensen M et al. *International Journal of Refractory Metals and Hard Materials*[J], 2006, 24(1-2): 135

Ti(C, N)-Mo₂C-Ni金属陶瓷与WC-Co硬质合金碱性条件下的冲刷腐蚀

邓成军^{1,2,3}, 林富凯³, 杨天恩^{3,4}, 洪华平⁴, 梁磊³, 彭华备³, 熊计³

(1. 重庆三峡学院 重庆市轻合金材料与加工工程技术研究中心, 重庆 404100)

(2. 重庆三峡学院 智能制造先导技术重庆市高校工程研究中心, 重庆 404100)

(3. 四川大学 机械工程学院, 四川 成都 610065)

(4. 宁波三韩合金材料有限公司, 浙江 宁波 315311)

摘要: 作为碱性条件下的抗磨蚀材料, WC-Co硬质合金所用的金属粘结剂Co属于可能致癌的物质, 并且钴尘可引起“硬金属病”, 因此有必要寻找可代替材料。采用Ti(C, N)-Mo₂C-Ni金属陶瓷作为抗磨蚀材料, 通过碱性条件下的电化学腐蚀和冲刷腐蚀, 观察了这两种材料的微观组织变化, 并比较了腐蚀速率及体积损失速率, 分析了材料表面破坏和体积损失机制。结果表明, 在NaOH溶液电化学腐蚀作用下, Ti(C, N)-Mo₂C-Ni金属陶瓷呈现了钝化现象, 其腐蚀表面的氧含量显著升高; 金属陶瓷的腐蚀速率比硬质合金小一个数量级。在碱性的砂-水混合液冲刷腐蚀作用下, 随冲刷时间增加, 金属陶瓷和硬质合金的体积损失速率都缓慢增加。在冲刷过程中, 金属陶瓷微观组织的环形相脆性大, 裂纹容易穿过环形相, 而芯相保持完整; 中粒度硬质合金中穿晶断裂模式较为常见; 细粒度硬质合金中裂纹多沿相界扩展。金属陶瓷和硬质合金在碱性的砂-水混合液冲刷腐蚀过程中, 砂粒冲刷磨损破坏作用是主要的。碱性的砂-水混合液冲刷腐蚀是腐蚀与冲刷两种作用相互影响、相互促进的加速破坏过程。已证实, 采用金属陶瓷代替硬质合金作为碱性条件的抗磨蚀材料是可行的, 且具有一定的优势。

关键词: 金属陶瓷; 硬质合金; 冲刷腐蚀; 电化学腐蚀; 碱性条件

作者简介: 邓成军, 男, 1983年生, 硕士, 重庆三峡学院重庆市轻合金材料与加工工程技术研究中心, 重庆 404100, E-mail: 273088644@qq.com